Fission of Pre-Actinide Nuclei near Stability

Tony Tran[1,*], *Kaitlin* J. Cook[1], *Jacob* Buete[1], *David* J. Hinde[1], *Mahananda* Dasgupta[1], *Lauren* T. Bezzina[1,**], *Dongyun* Y. Jeung[1], *Hyeonseop* Lee[1], and *Patrick* McGlynn[2,***]

[1]Department of Nuclear Physics and Accelerator Applications, Research School of Physics, The Australian National University, Canberra, ACT 2601, Australia
[2]Department of Fundamental and Theoretical Physics, Research School of Physics, The Australian National University, Canberra, ACT 2601, Australia

Abstract. We present preliminary results from a systematic study of heavy-ion induced fission fragment mass-total kinetic energy distributions for compound nuclei ranging from ^{203}Tl to ^{217}Fr. The data indicate shell effects present in the actinide region persist for all measured nuclides and offers the first model-independent observation of fission modes Standard I and Standard II in ^{203}Tl. Fission fragment mass and total kinetic energy distributions were analysed using a 2D fitting procedure. A systematic trend in the residuals between the data and the fitted model, which is comprised of the liquid drop mode with contributions from Standard I and Standard II, demonstrate the requirement of at least one more shell-driven fission mode closer to symmetry. This points towards at least one more deformed shell effect playing a substantial role in the fission of pre-actinide nuclei near stability.

1 Introduction

It has been more than eighty years since the discovery of nuclear fission [1], yet a comprehensive theoretical description remains elusive due to the inherently quantum many-body character of fission. The division of a single nucleus into two fission fragments can be modelled classically as the splitting of a charged liquid drop [2]. In this macroscopic picture, the energetics between Coulomb repulsion and nuclear surface tension favour the formation of fragments of similar mass, leading to mass-symmetric fission. However, it has been known since the discovery of fission that mass-asymmetric fission is observed in actinide nuclei — a feature now understood to arise from microscopic quantum effects in the nascent fragments.

The fission of actinide nuclei (Z = 89-103) has long been empirically associated with proton numbers near Z = 52.5 and Z = 55 in the heavy fragment [3, 4]. These fission modes have been termed Standard I (StI) and Standard II (StII) [5]. Recent theoretical calculations suggest that these modes are associated with proton numbers Z = 52 and 56, arising from octupole deformed shell gaps in the heavy fragment [6]. The observation of diminishing mass-asymmetric fission yields with decreasing compound nucleus proton number [4] led to the longstanding belief that fission of pre-actinide nuclei could be described by the liquid-drop model alone.

This belief was challenged by the unexpected observation of mass-asymmetric fission in neutron-deficient ^{180}Hg [7]. The subsequent demonstration [8, 9] that heavy-ion induced fission provided a viable pathway for observing mass-asymmetric fission, despite the expected damping of shell effects with increasing excitation energies (E_x), thus opened the door to a broader exploration of fission in this region. Recent surveys in the neutron deficient sub-lead region have found evidence of mass-asymmetric fission correlated with at least one of the following proton shells near Z = 34, 36 and Z = 44, 46 [10–16]. However, the unambiguous identification of which fission modes are present and their associated shell gaps remain an area of active investigation.

Of essential relevance to disambiguating these findings is the fission of pre-actinide nuclei near β-stability. Because of their proximity to both actinide and neutron-deficient sub-lead nuclei, they are expected to exhibit the characteristic fission modes present in both regions. Early measurements by Itkis *et al.* [17] observed mass-asymmetric fission. The fragment mass distributions near symmetry exhibited a double-humped structure, which was interpreted as a shell effect modifying the liquid drop potential energy, but might now be characterised as evidence for an asymmetric fission mode. At the extremes of the mass distributions, a mass-asymmetric fission mode with evidence of "fine structure" was also reported. This was observed to diminish in yield with decreasing compound nucleus proton number (Z_{CN}) and vanish for ^{201}Tl. A subsequent reanalysis of these data [18] concluded that fission in this region was governed by deformed neutron shells near N = 52 and N = 68. However, more recent

*e-mail: Tony.Tran@anu.edu.au
**Present address: Laboratory of Ion Beam Physics, ETH Zürich, Switzerland
***Present address: Facility for Rare Isotope Beams, Michigan State University, MI 48824, USA

measurements of ^{205,207,209}Bi have suggested possible shell effects near Z = 38, 45 and N = 56 [16].

To clarify these discrepancies, we present a systematic analysis of fission from ^{203}Tl to ^{217}Fr, investigating the number and characteristic properties of their fission modes. These measurements were acquired with statistics up to an order of magnitude larger than those of past studies in this region [17] and employ a substantially more comprehensive analysis procedure. Preliminary results hint at the presence of at least one more asymmetric fission mode in addition to StI and StII which are observed throughout.

2 Experiment

The measurements were carried out at the Heavy Ion Accelerator Facility at the Australian National University. Pulsed beams of ^{7}Li and ^{11}B with a FWHM of approximately 700 ps were delivered by the 14UD tandem electrostatic accelerator onto isotopically enriched targets (see Table 1). Projectile–target combinations were chosen to form compound nuclei near stability with N/Z ≈ 1.5. Beam energies were selected to minimise E_x while maintaining high fusion–fission cross sections. Fission fragments were detected in coincidence using the CUBE fission spectrometer [20], comprised in this case of two (279 × 357 mm^2 active area) multiwire proportional counters (MWPCs). The front MWPC was centred at laboratory angle 45°, while the back detector was at 123.75°. Fission fragment mass ratio ($M_R = M_1/(M_1 + M_2)$) and total kinetic energy (TKE) were reconstructed via the kinematic coincidence method [20].

Table 1: Summary of reactions studied, showing the beam-target combination, the resulting fissioning compound nucleus (CN), its neutron to proton ratio N/Z, the centre of mass energy E_{CM} corrected for energy loss through the first half of the target, the excitation energies above the ground state of the compound nucleus E_x, and the excitation energy above the calculated fission barrier [19] B_{fis}.

Reaction	CN	N/Z	E_{CM} (MeV)	E_x (MeV)	E_x-B_{fis} (MeV)
^{11}B + ^{206}Pb	^{217}Fr	1.494	49.30	29.86	17.12
^{7}Li + ^{209}Bi	^{216}Rn	1.512	33.82	30.21	15.97
^{7}Li + ^{206}Pb	^{213}At	1.506	33.84	31.54	12.98
^{11}B + ^{197}Au	^{208}Po	1.476	49.17	44.16	23.36
^{11}B + ^{196}Pt	^{207}Bi	1.494	52.96	49.03	26.75
^{7}Li + ^{197}Au	^{204}Pb	1.488	33.77	42.65	20.74
^{11}B + ^{192}Os	^{203}Tl	1.506	56.68	55.23	31.19

3 Analysis and Results

Panels (a) and (d) of Figure 1 show the M_R-TKE distributions for the heaviest and lightest nuclei in this study. There is an approximately parabolic dependence of the TKE on mass-split. Following Ref. [21, 22], the expected dependence of on mass-split was calculated, referred to as TKE_{Viola} [23], and is shown by the black solid line. To simplify the 2D fitting, we define the relative total kinetic energy, RTKE = TKE / TKE_{Viola}, which removes the

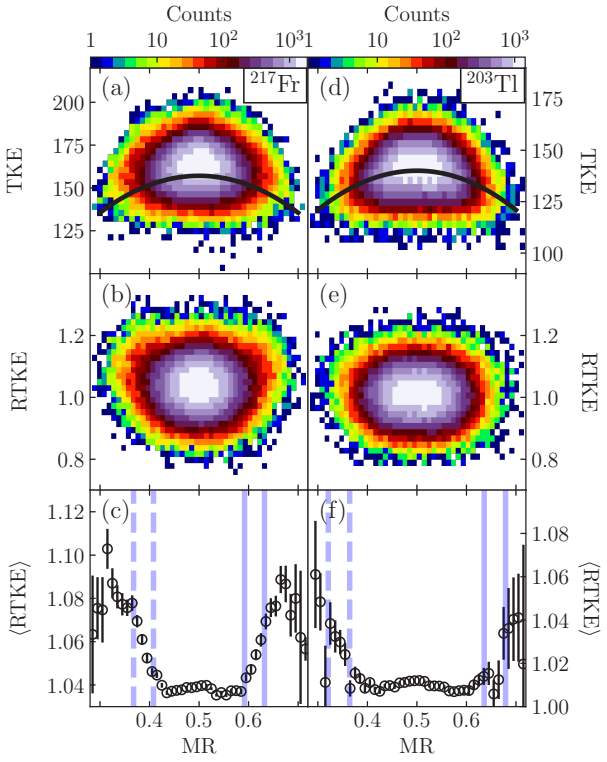

Figure 1: Experimental results for ^{217}Fr and ^{203}Tl, the heaviest and lightest nuclides studied. Panels (a) and (d) show the M_R-TKE spectra, panel (b) and (e) present the RTKE as a function of M_R, and panels (c) and (f) display the ⟨RTKE⟩ as a function of M_R. The blue solid bands represent the expected locations of St1 and St2 (Z = 51.5 and Z = 55) in M_R. The blue dashed lines represent the complementary fragment M_R's of StI and StII.

parabolic dependence on M_R. These 2D spectra of M_R against RTKE are shown in panels (b) and (e). Panels (c) and (f) show the average RTKE, ⟨RTKE⟩, for each M_R bin. The blue lines correspond to the M_R values of StI and StII (Z = 51.5 and 55) calculated following the unchanged charge density (UCD) assumption [24].

For one fission mode, if the fragment deformations are independent of M_R, the ⟨RTKE⟩ for that fission mode should be constant as a function of M_R. Thus, the dependence of the ⟨RTKE⟩ on M_R provides valuable insight towards disentangling fission modes. The ⟨RTKE⟩ for all systems measured in this work vary significantly with M_R, indicating the presence of multimodal fission. They all however, share a common "w-shaped" structure, highlighted in panels (c) and (f). The ⟨RTKE⟩ exhibits a local maximum at mass-symmetry, local minima on either side of symmetry, and then a strong rise at more asymmetric mass splits.

3.1 Observation of StI and StII

In panel (c), the contributions from StI and StII for ^{217}Fr are evident from the increase in the ⟨RTKE⟩ for $M_R > 0.58$ and at complementary fragment masses.

For ^{203}Tl, the ⟨RTKE⟩ for each bin in M_R, shown in panel (f), also shows a rise (though smaller) at large mass asymmetries where we expect to see the effects of StI and StII. This rise was also observed for all intermediate systems. This demonstrates that the standard fission modes persist at excitation energies as high as 31 MeV above the fission barrier for ^{203}Tl. Past measurements of the fission of the nearby isotope ^{201}Tl at an excitation of 9.5 MeV showed no indications of mass-asymmetric fission near the expected locations of StI and StII [17]. The qualitative evaluation of the ⟨RTKE⟩ provides a model-independent, data-driven signature of StI and StII for ^{203}Tl. By extension, this result suggests that, at the very least StI (as it is closer to symmetry than StII) is likely to be observed in the fission of nuclei lighter than ^{203}Tl until the energetic cost of extremely mass-asymmetric shape deformation exceeds the effect of shell stabilisation provided by the Z = 52 shell gap.

In addition to the rise at the extremes of mass-asymmetry, we also see local minima on either side of symmery in the ⟨RTKE⟩ for both nuclei. This can be seen near $M_R \sim 0.55$ in ^{217}Fr, near $M_R \sim 0.58$ in ^{203}Tl, and at their respective complimentary M_R values 0.45 and 0.42. This suggests the existence of one or more shell-driven fission modes moving outward from symmetry as the fissioning nucleus becomes lighter. To disentangle overlapping contributions from the liquid drop mode (LDM) and other shell driven modes close to symmetry, we require a quantitative and rigorous analysis approach.

3.2 Evidence for another fission mode

We want to know what additional fission mode(s) are present in our data, and what are their characteristics. By fitting *both* the M_R and RTKE simultaneously, we may disentangle fission modes that overlap in M_R but are sufficiently different in their RTKE, thereby identifying the number of fission modes and their characteristics.

The model used to represent each fission mode consists of a two-dimensional Gaussian in both M_R and RTKE. A symmetric mode is described by a single Gaussian centred at mass-symmetry, whereas an asymmetric mode is described by two Gaussians positioned at complementary mass splits. The total distribution is thus represented by a sum of 2D Gaussians [21]. Owing to the number of free parameters of the model and the correlations between them, the behaviour of any goodness-of-fit metric across the multidimensional parameter space becomes highly complex, leading to a challenging global optimisation problem. Furthermore, because the statistical uncertainties are Poissonian for bins with low counts, the traditional χ^2 metric is not appropriate, as it implicitly assumes Gaussian-distributed errors. To address these issues, the negative log-likelihood [25] is adopted as the goodness-of-fit statistic, where each bin is treated as a Poisson-distributed observation. In our work the model fit parameters are obtained through global optimisation using a generalised simulated annealing algorithm [26].

For nuclides with Z < 85, the global optimisation procedure does not detect contributions from StI and StII in the tails of the M_R-RTKE distributions. Their comparatively low statistics make them especially vulnerable to being overwhelmed by contributions from random statistical fluctuations closer to symmetry. However, insensitivity does not imply absence. We know StI and StII are present in all measurements from the analysis of the ⟨RTKE⟩. We may then impose constraints on their model parameters to prevent their relatively weak yield from being misattributed to adjacent asymmetric fission modes closer to mass-symmetry. The M_R centroids are fixed at the M_R values corresponding to the empirical mean proton numbers Z = 52.5 and 55 [3] and the widths are constrained to match those extracted for ^{217}Fr where StI and StII are most intense and their parameters could be reliably determined from the present experimental data. While some variation in the widths with excitation energy above the fission barrier is expected, this treatment is adequate given the small yields associated with these modes. And lastly, to ensure that the fitted modes actually correspond to StI and StII, the ordering of the RTKE centroids of the fit were required to match the empirically observed ordering, $\mathrm{RTKE_{StI}} > \mathrm{RTKE_{StII}} > \mathrm{RTKE_{LDM}}$ [27]. To explore

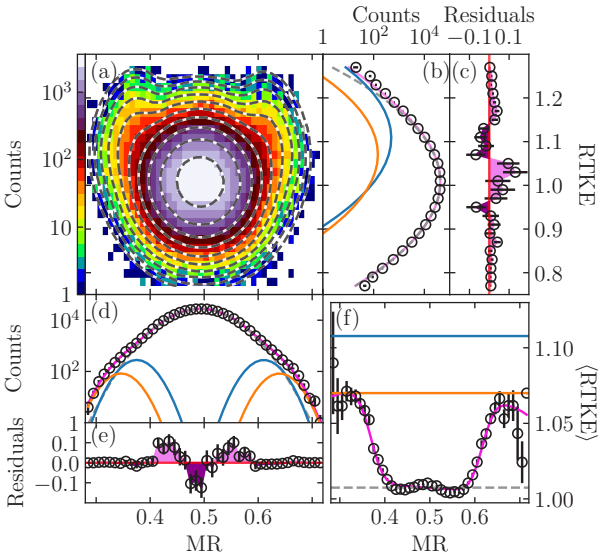

Figure 2: The best fit for ^{216}Rn. (a) The M_R-RTKE distribution and the fit. The dashed contours belong to the fit comprised of only StI, StII and a mass-symmetric mode. (b) The projection of the experimental data and fit onto the RTKE axis. The hollow circles are the experimental data, the grey dashed line is the symmetric contribution, the blue and orange curves represent contributions from StI and StII respectively, and the magenta line is the sum of the fission modes. (c) Residuals between the experimental data and fit for the RTKE projection. (d) The projection of the experimental data and fit onto the M_R axis. Lines have the same meaning as in (b). (e) Residuals between the experimental data and fit for the M_R projection. (f) Average RTKE as a function of M_R. Lines correspond to the average RTKE for each mode described as in (b)

evidence for a mass-asymmetric mode between symmetry and the known StI and StII modes, the 2D distributions were fitted *without* such a mode. The systematic evolution of the fit *residuals* across nuclides was then examined to obtain evidence for the presence of additional fission modes. The best fit for ^{216}Rn is shown in Fig. 2. Although this appears to be a good fit, there is a clear structure present in the residuals between the data and the fit in both the M_R and RTKE, seen in panels (c) and (e) respectively. This is due to the failure of the single Gaussian centred at symmetry to capture contributions from both the LDM and any additional mass-asymmetric shell-driven modes. The global optimisation process was carried out independently for each system. A consistent pattern emerges across all results. Fitting StI and StII together with a single symmetric mode fails to reproduce experiment for all measurements. Figure 3 shows the two-dimensional M_R-RTKE residuals (experimental data minus the optimal fit). Pronounced residual peaks (pink) and valleys (green) persist across all measured nuclei, together revealing a systematic trend that starts near mass-symmetry in ^{217}Fr and shifts progressively outward as the proton number of the compound nucleus decreases. This indicates the existence of at least one more shell-driven fission mode common to all systems. The location of the pink residual peaks, located near symmetry for ^{217}Fr (Z = 87) and at $M_R \approx 0.56$ (Z≈45) for ^{203}Tl (Z = 81) suggest the influence of proton shell gaps near Z = 44 and 46.

The locations of these residuals do not reveal the precise underlying shell effects. Their positions are influenced by the extent to which the symmetric liquid-drop component compensates for contributions from any underlying inner asymmetric mode. As the relative yields of the fission modes depend on the excitation energy above the fission barrier, which vary from system to system, the residuals cannot reliably tell us if the same shell can explain all the fit residuals. However, having established that a real shell effect is present, we may now fit another fission mode and repeat the residual analysis process. This work is ongoing and will be featured in a future paper. The consistency of the emerging correlations observed here strongly motivate further dedicated analysis, which will clarify the role of these shell effects in driving asymmetric fission near lead.

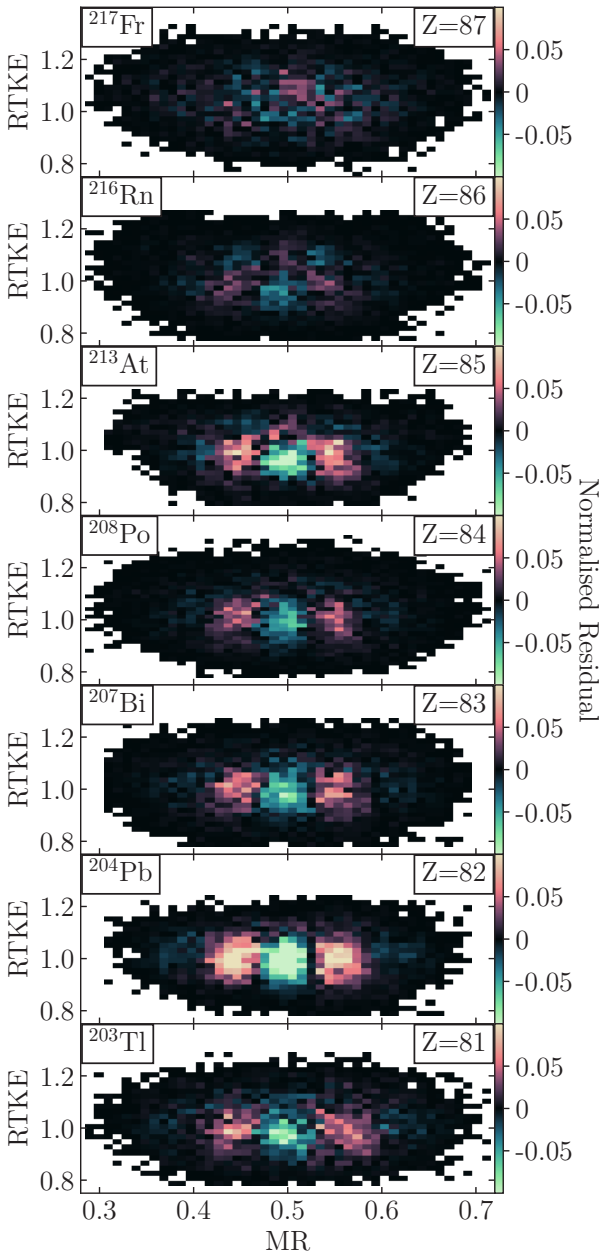

Figure 3: M_R–RTKE residuals between the experimental data and the fit for all systems, performed with the StI and StII modes constrained with a single symmetric mode. Positive residuals are shown in pink, and negative residuals in green, revealing a systematic failure of the constrained fit to fully reproduce the data. The colour scale expresses the residual normalised by the total number of counts and expressed as a percentage.

4 Conclusion

A high-statistics and rigorous 2D analysis of heavy-ion induced fission fragment mass–total kinetic energy distributions from ^{203}Tl to ^{217}Fr reveals a consistent underlying structure across pre-actinide nuclei near stability. The effects of StI and StII modes are observed for all systems studied. The systematic evolution of the M_R-RTKE residual distributions, obtained by comparing the data with a fit including only StI, StII, and a mass-symmetric mode, suggest the possible influence of deformed shell gaps near proton numbers Z = 44 and Z = 46. These findings provide new insight into what was once thought to simply be a transition from asymmetric fission in the actinides to symmetric fission in the pre-actinides, and highlight the need for further theoretical and experimental work to quantify the relative contributions of these shell effects and their evolution with excitation energy.

Acknowledgements

The authors acknowledge support from the Australian Research Council through Discovery Grants No. DP200100601, No. DP230101028, No. DE230100197, and No. DP250101791. Support for the Heavy Ion

Accelerator Facility operations from the Australian National Collaborative Research Infrastructure (NCRIS) HIA project is acknowledged. T.T and H.L. acknowledge support from the Australian Government Research Training Program (RTP) Scholarship. We thank Ryan Leknys, Damien McGinnes, Heiko Timmers, Lachlan McKie, and Martha Reece for their contribution towards running the experiment.

References

[1] L. Meitner and O. R. Frisch, Disintegration of Uranium by Neutrons: a New Type of Nuclear Reaction. Nature **143**, 239–240 (1939). https://doi.org/10.1038/143239a0

[2] N. Bohr and J. A. Wheeler, The Mechanism of Nuclear Fission. Physical Review **56**, 426–450 (1939). https://doi.org/10.1103/PhysRev.56.426

[3] C. Böckstiegel et al., Nuclear-fission studies with relativistic secondary beams: Analysis of fission channels. Nuclear Physics A **802**, 12–25 (2008). https://doi.org/10.1016/j.nuclphysa.2008.01.012

[4] K. H. Schmidt et al., Relativistic radioactive beams: A new access to nuclear-fission studies. Nuclear Physics A **665**, 221–267 (2000). https://doi.org/10.1016/S0375-9474(99)00384-X

[5] U. Brosa, S. Grossmann, and A. Müller, Nuclear scission. Physics Reports **197**, 167–262 (1990). https://doi.org/10.1016/0370-1573(90)90114-H

[6] G. Scamps and C. Simenel, Impact of pear-shaped fission fragments on mass-asymmetric fission in actinides. Nature **564**, 382–385 (2018). https://doi.org/10.1038/s41586-018-0780-0

[7] A. N. Andreyev et al., New Type of Asymmetric Fission in Proton-Rich Nuclei. Physical Review Letters **105**, 252502 (2010). https://doi.org/10.1103/PhysRevLett.105.252502

[8] K. Nishio et al., Excitation energy dependence of fragment-mass distributions from fission of ^{180,190}Hg formed in fusion reactions of ^{36}Ar +^{144,154} Sm. Physics Letters B **748**, 89–94 (2015). https://doi.org/10.1016/j.physletb.2015.06.068

[9] E. Prasad et al., Observation of mass-asymmetric fission of mercury nuclei in heavy ion fusion. Physical Review C **91**, 064605 (2015). https://doi.org/10.1103/PhysRevC.91.064605

[10] E. Prasad et al., Systematics of the mass-asymmetric fission of excited nuclei from ^{176}Os to ^{206}Pb. Physics Letters B **811**, 135941 (2020). https://doi.org/10.1016/j.physletb.2020.135941

[11] K. Mahata et al., Evidence for the general dominance of proton shells in low-energy fission. Physics Letters B **825**, 136859 (2022). https://doi.org/10.1016/j.physletb.2021.136859

[12] E. M. Kozulin et al., Fission of ^{180,182,183}Hg* and ^{178}Pt* nuclei at intermediate excitation energies. Physical Review C **105**, 014607 (2022). https://doi.org/10.1103/PhysRevC.105.014607

[13] A. A. Bogachev et al., Asymmetric and symmetric fission of excited nuclei of ^{180,190}Hg and ^{184,192,202}Pb formed in the reactions with ^{36}Ar and ^{40,48}Ca ions. Physical Review C **104**, 024623 (2021). https://doi.org/10.1103/PhysRevC.104.024623

[14] J. Buete et al., Universality of shell effects in fusion-fission mass distributions. Physics Letters B **865**, 139459 (2025). https://doi.org/10.1016/j.physletb.2025.139459

[15] P. Morfouace et al., An asymmetric fission island driven by shell effects in light fragments. Nature **641**, 339–344 (2025). https://doi.org/10.1038/s41586-025-08882-7

[16] B. M. A. Swinton-Bland et al., Mass-asymmetric fission of ^{205,207,209}Bi at energies close to the fission barrier using proton bombardment of ^{204,206,208}Pb. Physical Review C **102**, 054611 (2020). https://doi.org/10.1103/PhysRevC.102.054611

[17] M. G. Itkis et al., Asymmetric fission of the pre-actinide nuclei. Zeitschrift für Physik A Atoms and Nuclei **320**, 433–441 (1985). https://doi.org/10.1007/BF01415720

[18] S. I. Mulgin et al., Shell effects in the symmetric-modal fission of pre-actinide nuclei. Nuclear Physics A **640**, 375–388 (1998). https://doi.org/10.1016/S0375-9474(98)00332-7

[19] P. Möller et al, Fission barriers at the end of the chart of the nuclides. Physical Review C **91**, 024310 (2015). https://doi.org/10.1103/PhysRevC.91.024310

[20] D. J. Hinde et al., Conclusive evidence for the influence of nuclear orientation on quasifission. Physical Review C **53**, 1290–1300 (1996). https://doi.org/10.1103/PhysRevC.53.1290

[21] B. M. A. Swinton-Bland et al., Multi-modal mass-asymmetric fission of ^{178}Pt from simultaneous mass-kinetic energy fitting. Physics Letters B **837**, 137655 (2023). https://doi.org/10.1016/j.physletb.2022.137655

[22] D. J. Hinde et al., Neutron emission as a probe of fusion-fission and quasifission dynamics. Physical Review C **45**, 1229–1259 (1992). https://doi.org/10.1103/PhysRevC.45.1229

[23] V. E. Viola, K. Kwiatkowski, and M. Walker, Systematics of fission fragment total kinetic energy release. Physical Review C **31**, 1550–1552 (1985). https://doi.org/10.1103/PhysRevC.31.1550

[24] A. C. Wahl et al., Nuclear-Charge Distribution in Low-Energy Fission. Physical Review **126**, 1112–1127 (1962). https://doi.org/10.1103/PhysRev.126.1112

[25] A. C. Cameron and P. K. Trivedi, Regression Analysis of Count Data (Cambridge University Press, Cambridge, 2013), 71–72.

[26] Y. Xiang et al., Generalized simulated annealing algorithm and its application to the Thomson model. Physics Letters A **233**, 216–220 (1997). https://doi.org/10.1016/S0375-9601(97)00474-X

[27] S. I. Mulgin et al., The modal structure of fragment mass and energy yields from the 10.3–30.0 MeV proton induced fission of ^{232}Th and ^{235}U. Nuclear Physics A **824**, 1–23 (2009). https://doi.org/10.1016/j.nuclphysa.2009.03.013